Annals of Biomedical Engineering, Vol. 36, No. 5, May 2008 (© 2008) pp. 852–864
DOI: 10.1007/s10439-008-9463-6

Modeling the Nonlinear Dynamic Interactions of Afferent Pathways in the Dentate Gyrus of the Hippocampus

ANGELIKA DIMOKA,[1] SPIROS H. COURELLIS,[2] VASILIS Z. MARMARELIS,[2] and THEODORE W. BERGER[2,3]

[1]247A Bourns Hall, Department of Bioengineering, Bourns College of Engineering, University of California, Riverside, Riverside, CA 92521, USA; [2]Department of Biomedical Engineering, Viterbi School of Engineering, University of Southern California, Los Angeles, CA 90089-1111, USA; and [3]Neuroscience Program, University of Southern California, Los Angeles, CA 90089-2520, USA

(*Received 23 October 2007; accepted 6 February 2008; published online 26 February 2008*)

Abstract—The dentate gyrus is the first region of the hippocampus that receives and integrates sensory information (e.g., visual, auditory, and olfactory) via the perforant path, which is composed of two distinct neuronal pathways: the Lateral Perforant Path (LPP) and the Medial Perforant Path (MPP). This paper examines the nonlinear dynamic interactions among arbitrary stimulation patterns at these two afferent pathways and their combined effect on the resulting response of the granule cells at the dentate gyrus. We employ non-parametric Poisson–Volterra models that serve as canonical quantitative descriptors of the nonlinear dynamic transformations of the neuronal signals propagating through these two neuronal pathways. These Poisson–Volterra models are estimated in the so-called "reduced form" with experimental data from *in vitro* hippocampal slices and provide excellent predictions of the electrophysiological activity of the granule cells in response to arbitrary stimulation patterns. The data are acquired through a custom-made multi-electrode-array system, which stimulated simultaneously the two pathways with random impulse trains and recorded the neuronal postsynaptic activity at the granule cell layer. The results of this study show that significant nonlinear interactions exist between the LPP and the MPP that may be critical for the integration of sensory information performed by the dentate gyrus of the hippocampus.

Keywords—Hippocampus, Dentate gyrus, Perforant pathway, Poisson–Volterra, Kernel, Laguerre expansion, Multi input, Multi electrode.

INTRODUCTION

The hippocampus receives and integrates neuronal activity from multiple brain regions that are involved in processing different modalities of sensory information, especially in the context of learning and memory.[38,47] The primary function of the hippocampus is to form mnemonic labels that identify a unified collection of features to create semantic and temporal relations between multiple collections of features.[6,24] The different modalities of sensory information propagate through synaptic connections to converge onto a population of common postsynaptic neurons. These synaptic connections and the complex interactions of the sensory information are critical for the integrative functions of the hippocampus. However, due to the complexity and intrinsic nonlinearities of these interactions, the synaptic connections and the interactions of the different types of sensory information have not been adequately studied in the literature. A few researchers have attempted to model the multi-input interactions in the central nervous system[35,50] and other parts of the body,[15,18,44] while others have investigated the influence of prior synaptic activity on the subsequent induction of synaptic plasticity in the form of long term potentiation and long term depression in the dentate gyrus[1,22,59] or CA1.[34,58] In order to advance our understanding of the mechanisms that underlie learning and memory, we seek biologically interpretable models of how different modalities of sensory information are processed and integrated in the hippocampus.

Specifically, we focus on the functional interactions of two pathways on the dentate gyrus that represents the first integration level in the hippocampus (Fig. 1). The dentate gyrus receives its primary inputs from the entorhinal cortex via the perforant path, which consists of two distinct synaptic inputs/pathways, the lateral perforant path (LPP) and the medial perforant path (MPP), which receive and integrate cognitive information (e.g., visual, auditory, and olfactory) from other brain regions.[56,61] It is possible to isolate the LPP and the MPP experimentally, because they are anatomically and functionally distinct (Fig. 1).[30,31,53]

Address correspondence to Angelika Dimoka, 247A Bourns Hall, Department of Bioengineering, Bourns College of Engineering, University of California, Riverside, Riverside, CA 92521, USA. Electronic mail: dimoka@ucr.edu

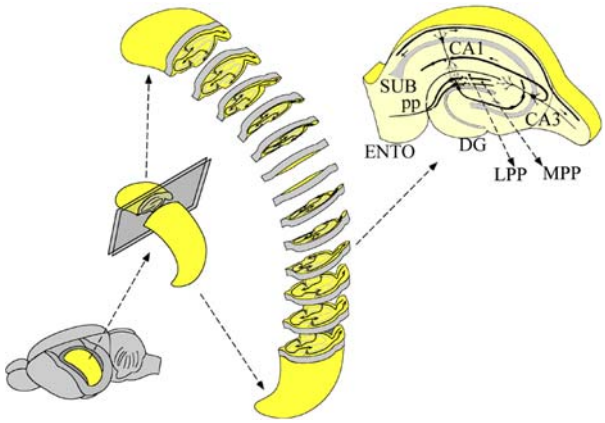

FIGURE 1. Schematic of the hippocampal circuitry. The perforant path of the dentate gyrus consists of two anatomically and functionally distinct subdivisions: the lateral perforant path (LPP) that arises in the ventrolateral entorhinal area and synapses in the outer one-third of the molecular layer, and the medial perforant path (MPP) that arises in the dorsomedial entorhinal cortex and synapses to the granule cell dendrites in the middle one-third of the molecular layer.

The LPP originates in the ventrolateral entorhinal area and generates synapses on the outer one-third of the molecular layer. The MPP arises in the dorsomedial entorhinal cortex and synapses on the granule cell dendrites in the middle one-third of the molecular layer. The synaptic responses elicited in granule cells by activation of these two distinct pathways exhibit a number of different physiological[2,46,45] and pharmacological[28,33,36] characteristics. The output of the dentate gyrus is subsequently processed in the hippocampus through several sub-regions that form a closed loop (see Fig. 1). These sub-regions primarily consist of cascaded excitatory connections that are organized roughly transverse to the longitudinal axis of the hippocampus, and they can be viewed as a set of interconnected, parallel circuits. The significance of this anatomical organization is that transverse slices (400 μm thick) of the dentate gyrus may be maintained *in vitro* and preserve a substantial portion of their intrinsic transverse circuitry.

Mathematical models have been developed on the basis of physiological and biophysical principles to characterize the functional properties of cortical areas.[32,55,60] These hypothesis-based models contain several parameters that are biologically interpretable and must be measured or estimated from experimental data (whereby the term ''parametric models''). The parametric models are not easy to scale-up in the case of multiple interconnected neuronal units or when the functional complexity of the system increases, because the number of parameters required to represent such functional complexity usually becomes too large for a workable model. To overcome this limitation, *non-parametric* models based on the input–output approach were introduced in the so-called ''reduced form'' about 20 years ago to offer a comprehensive functional representation of neuronal networks in the hippocampus.[9,10,14,49] More recently, non-parametric models have been used for modeling the input–output relationship in the dentate gyrus[11,7] or in the CA1 region[25] of the hippocampus. A recently accepted paper presents non-parametric models of the separate effects of LPP and MPP stimulation on the granule cell activity but does not examine the nonlinear interactions of the two inputs and their combined effect on granule cell activity.[21] In the present paper, we employ a ''reduced form'' non-parametric model based on the Poisson–Volterra approach[8,9,41,42] to model the *nonlinear dynamic interactions* of the simultaneous LPP and the MPP stimulation and the *combined effect* of the two inputs on the granule cell activity in the dentate gyrus of the hippocampus.

The Poisson–Volterra modeling approach is mathematically rigorous and yields canonical models with excellent predictive capabilities, even when the system exhibits complex nonlinear dynamics. The key features of these models are the *Poisson–Volterra kernels*, which are quantitative descriptors of the system function in terms of the input–output relationships and fully capture all possible nonlinear interactions among the underlying biological mechanisms.[41,42] These kernels can be estimated robustly from experimental input–output data and take the ''reduced form'' when the output population spike is synchronized with the input impulses.[8,9,49] The non-parametric models are data-based (inductive), unlike the parametric models that are hypothesis-based (deductive). In the context of this study, the non-parametric model has an advantage over its parametric counterparts since it represents the combined activities of *all* known and unknown components of neuronal interactions without any assumptions about the model structure and the numbers or types of elements that may be contributing to the neuronal activity. Most importantly, the non-parametric modeling approach can be extended to encompass the increasing complexity of multiple inputs and outputs that is emerging with the recent availability of multi-unit recordings using multi-electrode arrays.

In the present study, the LPP and MPP pathways were stimulated simultaneously with two independent sequences of impulses having a random (Poisson) distribution of inter-impulse intervals and the elicited response of a population of granule cells—the output of the neuronal system in this formulation—was recorded with the multi-electrode arrays that were used to simultaneously stimulate the LPP and the MPP. The employed stimulus is termed the Random Impulse

Train (RIT), and it has been shown to test the system with a variety of input patterns over a short experimental time in a manner that reveals all possible interactions within the system.[8,9,21,27,41,43] The collected experimental data were used to estimate in reduced form the Poisson–Volterra models for two inputs that include up to third-order nonlinear interactions between the LPP and the MPP. The results suggest that *third-order nonlinear interactions* (quantified by the *cross-kernels* in the model) must be included in the reduced-form Poisson–Volterra model to achieve adequate predictive accuracy during co-activation of the LPP and the MPP. The employed experimental and computational methods are presented in the following section. The results are presented in the subsequent section, followed by the Discussion section.

MATERIALS AND METHODS

Experimental Preparation

Thin slices were taken from the hippocampus of adult Sprague-Dawley male rats, 7–9 months of age using standard procedures.[21] Each slice was carefully positioned on a multi-electrode array over an inverted microscope (DML, DMIRB, Leika, Germany). The slice was positioned so that stimulating electrodes covered the inner blade of the dentate gyrus (Fig. 2a). Accurate positioning of the slice on top of the multi-electrode array was attained by floating the slice using a very fine hair brush. The positioning of the slice relative to the array was documented with a digital camera (Hitachi VK-C370, Spot Model 2.0.0). Throughout all experiments, slices were perfused with a 1 mM $MgSO_4$ aCSF (artificial Cerebro-Spinal Fluid) at a flow rate of 15 mL/min, and constantly heated at 33 °C. A multi-electrode array system was used to simultaneously stimulate and record from multiple sites in each hippocampal slice. The system consisted of two components: (1) a multi-site electrode array, and (2) a multi-channel stimulation-recording system. The multi-site electrode array employed in this experiment is custom-designed and was fabricated and tested in the Center for Neural Engineering at the University of Southern California.[21,27] The array was positioned so that its electrode sites cover the appropriate sub-regions of the dentate gyrus (LPP and MPP) with sufficient density as to allow separate stimulation of each pathway. The multi-electrode array has 60 microelectrodes in a 3×20 configuration. The microelectrodes are embedded in a planar glass plate and their diameter is 28 μm with a center-to-center spacing of 50 μm. The multi-channel stimulation-recording

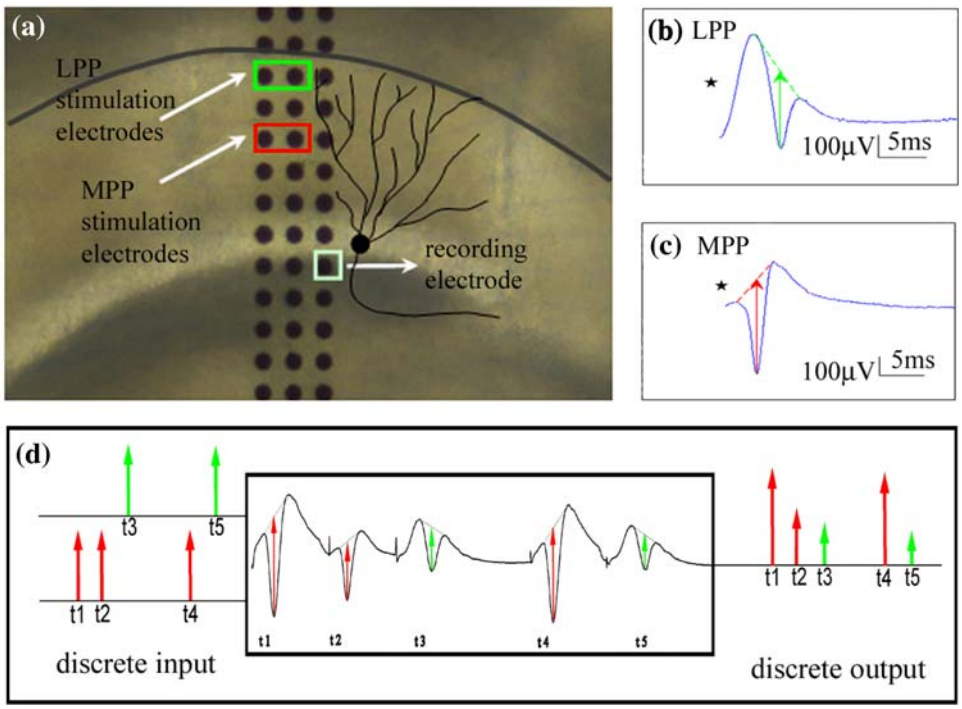

FIGURE 2. Selected electrodes for LPP and MPP stimulation (a). Characteristic field potential responses from the granule cell layer due to LPP stimulation (b) or MPP stimulation (c). The occurrence of the stimulation is denoted by ⋆. The negative-going deflection in each response is the population spike and its amplitude is measured as indicated by the vertical arrow. A segment of RIT input impulses (with randomly varying inter-impulse intervals) of the two point-process stimuli applied to LPP (green) and MPP (red) along with the elicited population spikes at the granule cells (d).

system is a commercially available product (MEA60 Multi Channel Systems, Germany) that consists of preamplifiers, data acquisition card, 8-channel stimulation box and software for data acquisition and preprocessing (MC Stimulus v2.0.3, MC Rack v 2.2.2).

Each slice was positioned on top of the multi-electrode array as to cover the molecular layer from the fissure to the granule cell body layer at the upper blade of the dentate gyrus. Electrodes positioned at the outer one-third of the molecular layer were chosen as candidates to stimulate the LPP and at the middle one-third of the molecular layer to stimulate the MPP. The selection of the optimum stimulating electrodes was confirmed by the following electrophysiological criteria: (1) field Excitatory Post-Synaptic Potentials (fEPSPs) showed paired-pulse facilitation when the LPP was stimulated, and paired-pulse depression when the MPP was stimulated;[16,33,39,45] (2) fEPSPs exhibited a dendritic current sink at the outer molecular layer and a dendritic current source at the middle molecular layer when LPP was stimulated (accordingly, when the MPP was stimulated fEPSPs exhibited a dendritic current sink at the middle molecular layer and a dendritic current source at the outer molecular layer);[16,20] (3) stimulation at MPP exhibited shorter latencies of the population spike recorded in the granule cell layer than when the LPP was stimulated.[8,10,45] The electrode positioned right below the granule cell layer into the hilus was used to record the electrophysiological activity of granule cells in the form of population spikes that reflect the synchronous activation of dentate granule cells.[3,37]

Experimental Protocol

At the beginning of each experiment, input–output (I/O) curves were recorded for the LPP and the MPP separately. Each pathway was stimulated with a series of pulses having intensities that varied between 10 and 140 μA, in 10 μA increments. Stimulation was delivered in the form of bi-phasic pulses (100 μs duration) via the pair of stimulation electrodes appropriate for each pathway. The time between successive pulses was set to 30 s to avoid induction of long-term potentiation. Each series of pulses was repeated five times. The I/O curve for each pathway was used to determine the value of the stimulation intensity that evoked 50% of the maximum population spike amplitude response in the granule cell layer. This value was used for the remainder of each experiment. Both pathways were simultaneously stimulated with random impulse train (RIT) stimuli. Each RIT contained 800 Poisson-distributed impulses (mean inter-impulse interval of 500 ms, covering the approximate range of 10–4000 ms). The parameter of the Poisson distribution that determines the average firing rate of the RIT was consistent with the known firing rates of the respective hippocampal neurons (2 Hz).[51,57] At the end of RIT stimulation, the system was tested for stationarity by administering a series of I/O curve stimulations. Possible differences in the resulting I/O curves before and after RIT stimulation were taken as indicators of changes in granule cell excitability (non-stationarity of the system). Only data that exhibited levels of such changes within $\pm 15\%$ of the baseline were included in the analysis.

The experimental data were sampled at 25 kHz per channel and the amplitude of each population spike was extracted for analysis using a customized interface written in Matlab (v6.5). The amplitude of the population spike was defined as the segment of the vertical line between the negative peak of the spike and the tangential straight line connecting the spike onset and offset (see Figs. 2b and 2c).

Poisson–Volterra Modeling of a Two-Input System

The collected data were analyzed using a variant of the general Volterra modeling approach[43,41,42] adapted to the two-input case. The two inputs are independent Poisson RIT stimuli and the output is the resulting sequence of population spikes with variable amplitude. This approach considers the input and the output spikes to be synchronized, i.e., to occur in the same time-bin which is set equal to 10 ms so that it exceeds the maximum output latency of 8.2 ms observed in our experiments.

The point-process inputs of the system (LPP and MPP) are RIT sequences of impulses expressed as:

$$x_{\mathrm{L}} = \sum_{n_{j_{\mathrm{L}}}} \delta(n - n_{j_{\mathrm{L}}}) \tag{1}$$

$$x_{\mathrm{M}} = \sum_{n_{j_{\mathrm{M}}}} \delta(n - n_{j_{\mathrm{M}}}) \tag{2}$$

where the discrete-time delta function (Kronecker delta) denotes an impulse at the indicated discrete time-index n_j, and the subscripts L and M denote the LPP and MPP pathways, respectively. The population spike amplitude that is generated in the granule cell layer in response to a stimulating impulse either at the LPP or the MPP is given by:

$$y(n_i) = y_{\mathrm{L}}(n_{i_{\mathrm{L}}}) + y_{\mathrm{M}}(n_{i_{\mathrm{M}}}) \tag{3}$$

where $y(n_i)$ is the output at discrete time n_i, which is the time of occurrence of the i-th stimulating impulse either at the LPP or the MPP. An implicit assumption is that stimulating impulses do not occur simultaneously at both pathways, so that only one pathway can be stimulated at each time instant n_i. In the

adopted modeling formulation, the output is composed of two components corresponding to the timing of the impulses of each of the two inputs that are given by the expressions of the reduced-form Poisson–Volterra model with two inputs as:

$$\begin{aligned} y_{\mathrm{L}}(n_{i_{\mathrm{L}}}) = {} & k_{1y_{\mathrm{L}}} + \sum_{n_{j_{\mathrm{L}}}} k_{2y_{\mathrm{L}}x_{\mathrm{L}}}(n_{i_{\mathrm{L}}} - n_{j_{\mathrm{L}}}) \\ & + \sum_{n_{j_{\mathrm{M}}}} k_{2y_{\mathrm{L}}x_{\mathrm{M}}}(n_{i_{\mathrm{L}}} - n_{j_{\mathrm{M}}}) \\ & + \sum_{n_{j_{\mathrm{L}}}} \sum_{n_{j'_{\mathrm{L}}}} k_{3y_{\mathrm{L}}x_{\mathrm{L}}x_{\mathrm{L}}}(n_{i_{\mathrm{L}}} - n_{j_{\mathrm{L}}}, n_{i_{\mathrm{L}}} - n_{j'_{\mathrm{L}}}) \\ & + \sum_{n_{j_{\mathrm{L}}}} \sum_{n_{j'_{\mathrm{M}}}} k_{3y_{\mathrm{L}}x_{\mathrm{L}}x_{\mathrm{M}}}(n_{i_{\mathrm{L}}} - n_{j_{\mathrm{L}}}, n_{i_{\mathrm{L}}} - n_{j_{\mathrm{M}}}) \\ & + \sum_{n_{j_{\mathrm{M}}}} \sum_{n_{j'_{\mathrm{M}}}} k_{3y_{\mathrm{L}}x_{\mathrm{M}}x_{\mathrm{M}}}(n_{i_{\mathrm{L}}} - n_{j_{\mathrm{M}}}, n_{i_{\mathrm{L}}} - n_{j'_{\mathrm{M}}}) \end{aligned} \tag{4}$$

and

$$\begin{aligned} y_{\mathrm{M}}(n_{i_{\mathrm{M}}}) = {} & k_{1y_{\mathrm{M}}} + \sum_{n_{j_{\mathrm{L}}}} k_{2y_{\mathrm{M}}x_{\mathrm{L}}}(n_{i_M} - n_{j_L}) \\ & + \sum_{n_{j_{\mathrm{M}}}} k_{2y_{\mathrm{M}}x_{\mathrm{M}}}(n_{i_2} - n_{j_2}) \\ & + \sum_{n_{j_{\mathrm{L}}}} \sum_{n_{j'_{\mathrm{L}}}} k_{3y_{\mathrm{M}}x_{\mathrm{L}}x_{\mathrm{L}}}(n_{i_{\mathrm{M}}} - n_{j_{\mathrm{L}}}, n_{i_{\mathrm{M}}} - n_{j'_{\mathrm{L}}}) \\ & + \sum_{n_{j_{\mathrm{L}}}} \sum_{n_{j'_{\mathrm{M}}}} k_{3y_{\mathrm{M}}x_{\mathrm{M}}x_{\mathrm{L}}}(n_{i_{\mathrm{M}}} - n_{j_{\mathrm{M}}}, n_{i_{\mathrm{M}}} - n_{j_{\mathrm{L}}}) \\ & + \sum_{n_{j_{\mathrm{M}}}} \sum_{n_{j'_{\mathrm{M}}}} k_{3y_{\mathrm{M}}x_{\mathrm{M}}x_{\mathrm{M}}}(n_{i_{\mathrm{M}}} - n_{j_{\mathrm{M}}}, n_{i_{\mathrm{M}}} - n_{j'_{\mathrm{M}}}) \end{aligned} \tag{5}$$

where the discrete-time index n_j over which summation occurs in the above expressions is the time of occurrence of any prior j-th impulse within a time window μ starting at present and extending into the past (termed the "system memory" and representing the input past epoch exerting causal effects on the output present value). Note that these prior impulses may occur at either stimulating pathway (LPP or MPP), as indicated by the respective subscript of the time index. Thus, a stimulating impulse at one pathway may exert a causal effect on the granule cells through either pathway over a subsequent time window equal to the system memory μ. The effects that are due to the same pathway are represented by the "self-kernels" and those due to the other pathway are represented by the "cross-kernels" (see below). These two sets of reduced-form Poisson–Volterra kernels are clearly separated and constitute the key features of this Poisson–Volterra model,[42] since they describe the quantitative effects of the inputs on the output and provide the model with its predictive capability. The estimation of these kernels using actual input–output data is the key objective of the modeling task in this context. In the expressions (4) and (5) above, the following reduced-form Poisson–Volterra kernels are denoted by the proper subscript for the respective input (L for LPP or M for MPP): $k_{1y_{\mathrm{L}}}$ and $k_{1y_{\mathrm{M}}}$ are the first-order kernels (constants), $k_{2y_{\mathrm{L}}x_{\mathrm{L}}}(n)$ and $k_{2y_{\mathrm{M}}x_{\mathrm{M}}}(n)$ are the second-order self-kernels (one dimensional), $k_{2y_{\mathrm{L}}x_{\mathrm{M}}}(n)$ and $k_{2y_{\mathrm{M}}x_{\mathrm{L}}}(n)$ are the second-order cross-kernels (one dimensional), $k_{3y_{\mathrm{L}}x_{\mathrm{L}}x_{\mathrm{L}}}n_1, n_2$ and $k_{3y_{\mathrm{M}}x_{\mathrm{M}}x_{\mathrm{M}}}(n_1, n_2)$ are the third-order self-kernels (two dimensional), and $k_{3y_{\mathrm{L}}x_{\mathrm{L}}x_{\mathrm{M}}}(n_1, n_2), k_{3y_{\mathrm{L}}x_{\mathrm{M}}x_{\mathrm{M}}}(n_1, n_2)$, $k_{3y_{\mathrm{M}}x_{\mathrm{M}}x_{\mathrm{L}}}(n_1, n_2)$ and $k_{3y_{\mathrm{M}}x_{\mathrm{L}}x_{\mathrm{L}}}(n_1, n_2)$ are the third-order cross-kernels (two dimensional). The obtained estimates of these kernels are shown in the following section.

The first-order kernel represents the amplitude of the population spike attributed to the respective input impulse when it is acting alone—i.e., in the absence of any other input impulse within the system memory. The second-order self-kernel represents the nonlinear dynamic interactions within a single pathway (either the LPP or the MPP) between the present impulse and each of the past impulses of the same stimulus within the memory window μ. These nonlinear dynamic interactions result in partial modulation of the output (the amplitude of the population spike) in a manner dictated by the specific value of the second-order self-kernel corresponding to the specific inter-impulse interval, in accordance with the reduced-form Poisson–Volterra model of Eqs. (3)–(5). Additional output modulation results from the other terms of the model in a manner dictated by the respective kernels. Thus, the second-order cross-kernel represents the nonlinear dynamic interactions across two pathways for the respective inter-impulse interval, i.e., between the present stimulus impulse in one pathway and each of the past stimulus impulses in the other pathway within the memory window μ.

In analogous fashion, the third-order self-kernel represents the interactions between the present impulse and any two preceding impulses of the same stimulus within a single pathway over the memory window μ, and the third-order cross-kernel represents the interactions between the present stimulus impulse in one pathway and any two preceding stimulus impulses in the other pathway over the memory window μ. The specific amount of third-order modulation of the output population spike is determined by the value of the respective third-order kernel at the corresponding two inter-impulse intervals. Therefore, knowledge of the values of these kernels provides complete quantitative information about the nonlinear functional characteristics of the system (for the respective order of interactions), including the manner in which the two pathways interact to integrate incoming information and produce the neuronal activity at the granule cells of the dentate gyrus.

In order to estimate efficiently and accurately the kernels from relatively short input–output data records, we approximate them with linear combinations of exponentially decaying Laguerre functions through an orthogonal expansion which improves the estimation accuracy and reduces the computational effort.[40] The Laguerre expansion coefficients are estimated using least-squares methods, and the kernel estimates are reconstructed using the respective estimated expansion coefficients.[17] The predictive accuracy of the obtained model (employing the estimated kernels) can be evaluated using the Normalized Mean Square Error (NMSE) of the model prediction vs. the actual output of the system, which is non-negative and defined as:

$$\mathrm{NMSE} = \frac{\sum_i (Y_{\mathrm{pr}_i} - Y_{\mathrm{data}_i})^2}{\sum_i^{Y^2_{\mathrm{data}_i}}} \qquad (6)$$

where Y_{pr} is the predicted amplitude of the population spikes using the estimated kernels and Y_{data} is the recorded amplitude of the population spikes obtained during the experiment. The value of the NMSE is taken as a measure of the predictive capability of the model and becomes zero for a perfect prediction. The inevitable presence of measurement errors and noise in the data prevents the NMSE from becoming zero in a practical context, even if the model is perfect. Therefore, the interpretation of the numerical values of the computed NMSE must be made in the context of the noise conditions and possible measurement errors in each case. Typically, NMSE values of less than 0.2 are deemed to indicate satisfactory predictive capability of the model that validates its specific form. Since the kernel estimation procedure employs Laguerre expansions, the NMSE value of the model prediction depends on the selected number of Laguerre functions for kernel expansion (L) and the value of the Laguerre parameter α.[41,42] The selection of the optimum values of α and L in each particular application is accomplished through a search procedure over various values of L and α (varying in ascending order) that seeks to minimize the NMSE of the respective model prediction. The number L of Laguerre functions is selected through the mentioned search procedure by requiring that an increase of L by 1 causes reduction of the prediction NMSE by at least 3%.

The kernel estimation procedure and the nonlinear modeling/analysis of this system were performed with the use of a specialized software package (LYSIS) that has been developed by the Biomedical Simulations Resource at the University of Southern California and is distributed to the biomedical community free of charge. The statistical significance of the obtained estimates of the Laguerre expansion coefficients (from which the kernel estimates and the Poisson–Volterra model predictions are constructed) was evaluated by applying the Student's t-test at the significance level of $p < 0.01$.

RESULTS

Five experiments were performed *in vitro* using RIT stimuli for the two inputs (LPP and MPP) and data records of 400 spikes per pathway for each experiment were collected. Following a search procedure of successive trials and using the prediction NMSE as criterion for model performance, we selected the third-order reduced-form Poisson–Volterra model described by Eqs. (3)–(5) as the most appropriate for the analysis the data collected in the RIT experiments. Three Laguerre functions ($L = 3$) were selected for the kernel expansions as a good compromise between prediction accuracy and model complexity (since the total number of free parameters increases with L). For $L = 3$, the total number of free parameters in the two-input model of Eqs. (4)–(5) is 62, which is less than a third of the number of output spikes and assures that we avoid the risk of overfitting. For $L = 3$, the optimum value of the Laguerre parameter $\alpha = 0.984 \pm 0.004$ was selected as to minimize the NMSE of the model prediction. Figure 3 shows the average NMSE derived from the five different experiments for $L = 3$ and a

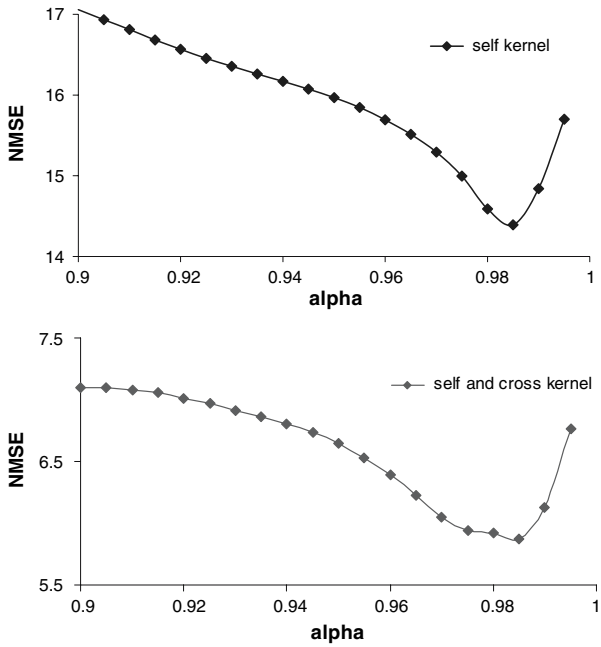

FIGURE 3. The average NMSE values over five experiments using the third-order Poisson–Volterra model given by Eqs. (3)–(5) for a range of α values from 0.90 to 0.99 and three Laguerre functions ($L = 3$). For the optimum selection of $\alpha = 0.984$ and $L = 3$, the NMSE of the model prediction is 14.39 ± 3.86% when only the self-kernels are included, and drops to 5.88 ± 2.51% when both self-kernels and cross-kernels are included in the model.

range of α values from 0.90 to 0.99. For these selections of L and α values, the NMSE was calculated both with and without including the cross- kernels in the third-order model. When only the self-kernels were included, the value of the NMSE was 14.39 ± 3.86%. When both the self-kernels and the cross-kernels were included the NMSE dropped to 5.88 ± 2.51%. The inclusion of the cross-kernels reduced the NMSE by 8.52%. Application of the paired t-test indicated that the inclusion of the cross- kernels resulted in a statistically significant reduction of the NMSE ($p < 0.01$), which implies that significant dynamic interactions exist between the two pathways.

For each input–output dataset, the first-order, second-order and third-order kernels were estimated for $L = 3$ and the optimum value of the parameter $\alpha = 0.984 \pm 0.002$. Over the five experiments, the average value (± one standard deviation) of the first-order kernel (k_{1y_L}) for the LPP was 186.75 μV (± 54.9 μV) and of the first-order kernel (k_{1y_M}) for the MPP was 276.65 μV (± 22.1 μV). The average values and the standard-deviation bounds of the second-order self-kernels and cross-kernels, normalized by the corresponding first-order kernel value, are shown in Fig. 4 for the LPP and in Fig. 5 for the MPP. It is evident in Fig. 4a that the average values of the normalized second-order LPP self- kernel $k_{2y_Lx_L}$ exhibit initially a fast facilitatory phase up to about 110 ms, followed by a slow inhibitory phase up to about 1600 ms. In Fig. 4b, the average values of the normalized second-order cross-kernel $k_{2y_Lx_M}$ exhibit initially a moderate facilitatory phase that crosses into a very shallow inhibitory phase around 200 ms and diminishes around 800 ms. By contrast, we observe in Fig. 5a that the average values of the normalized second-order MPP self-kernel $k_{2y_Mx_M}$ exhibit initially a very small facilitatory phase up to about 70 ms, followed by a slow inhibitory phase that diminishes around 1800 ms. In Fig. 5b, we see that the average values of the normalized second-order cross-kernel $k_{2y_Mx_L}$ exhibit initially a moderate facilitatory phase up to about 160 ms and cross into a shallow inhibitory phase that diminishes around 1200 ms. We observe the distinct dynamic characteristics of the self-kernels for the two input pathways and the similar dynamic characteristics of the cross-kernels.

The average values of the normalized third-order self-kernels and cross-kernels (as well as their respective standard-deviation bounds) are shown in Fig. 6

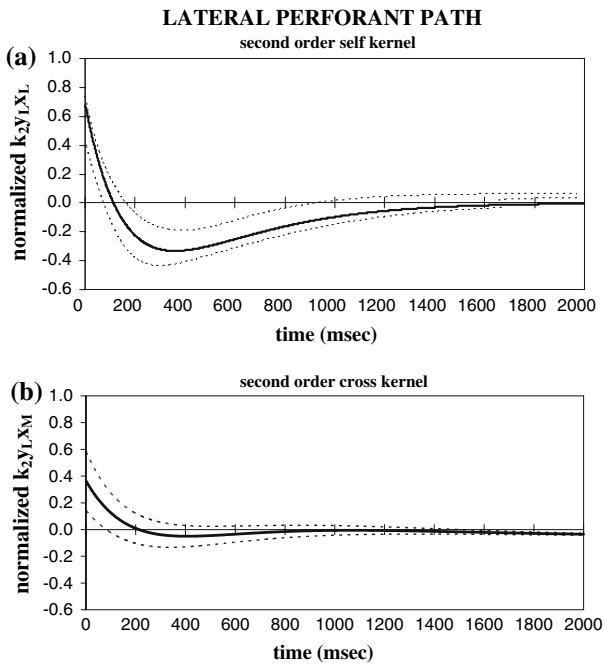

FIGURE 4. The average values of the normalized second-order self-kernel ($k_{2y_1x_1}$) and cross-kernel ($k_{2y_1x_2}$) for the LPP. The dotted line shows ±one standard deviation for five different experiments. In (a), the average values of the normalized self-kernel exhibit initially a fast facilitatory phase up to about 110 ms followed by a slow inhibitory phase up to about 1800 ms. In (b), the average values of the normalized cross-kernel exhibit initially a moderate facilitatory phase that crosses into a very shallow inhibitory phase shortly around 200 ms and diminishes around 800 ms.

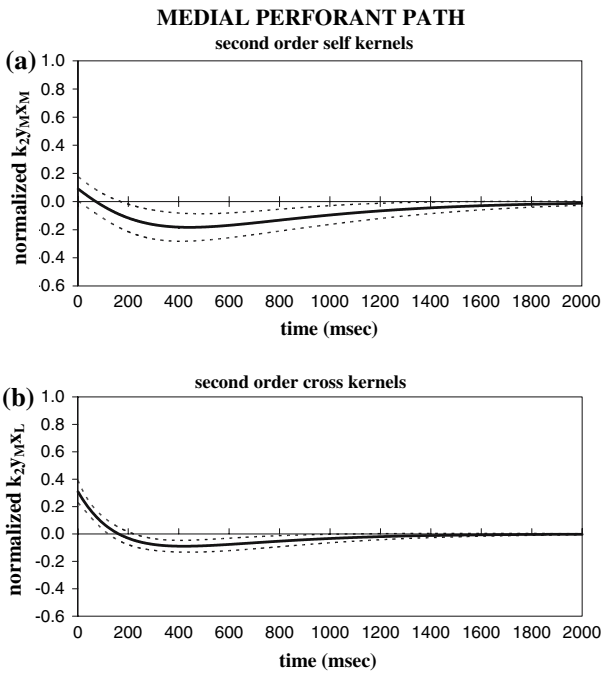

FIGURE 5. The average values of the normalized second-order self-kernel ($k_{2y_2x_2}$) and cross-kernel ($k_{2y_2x_1}$) for the MPP. The dotted line shows ±one standard deviation for the five different experiments. In (a), the average values of the normalized self-kernel exhibit initially a very small facilitatory phase up to about 70 ms, followed by a slow inhibitory phase that diminishes around 1800 ms. In (b), the average values of the normalized cross-kernel $k_{2y_2x_1}$ exhibit initially a moderate facilitatory phase up to about 160 ms and cross into a shallow inhibitory phase that diminishes around 1200 ms.

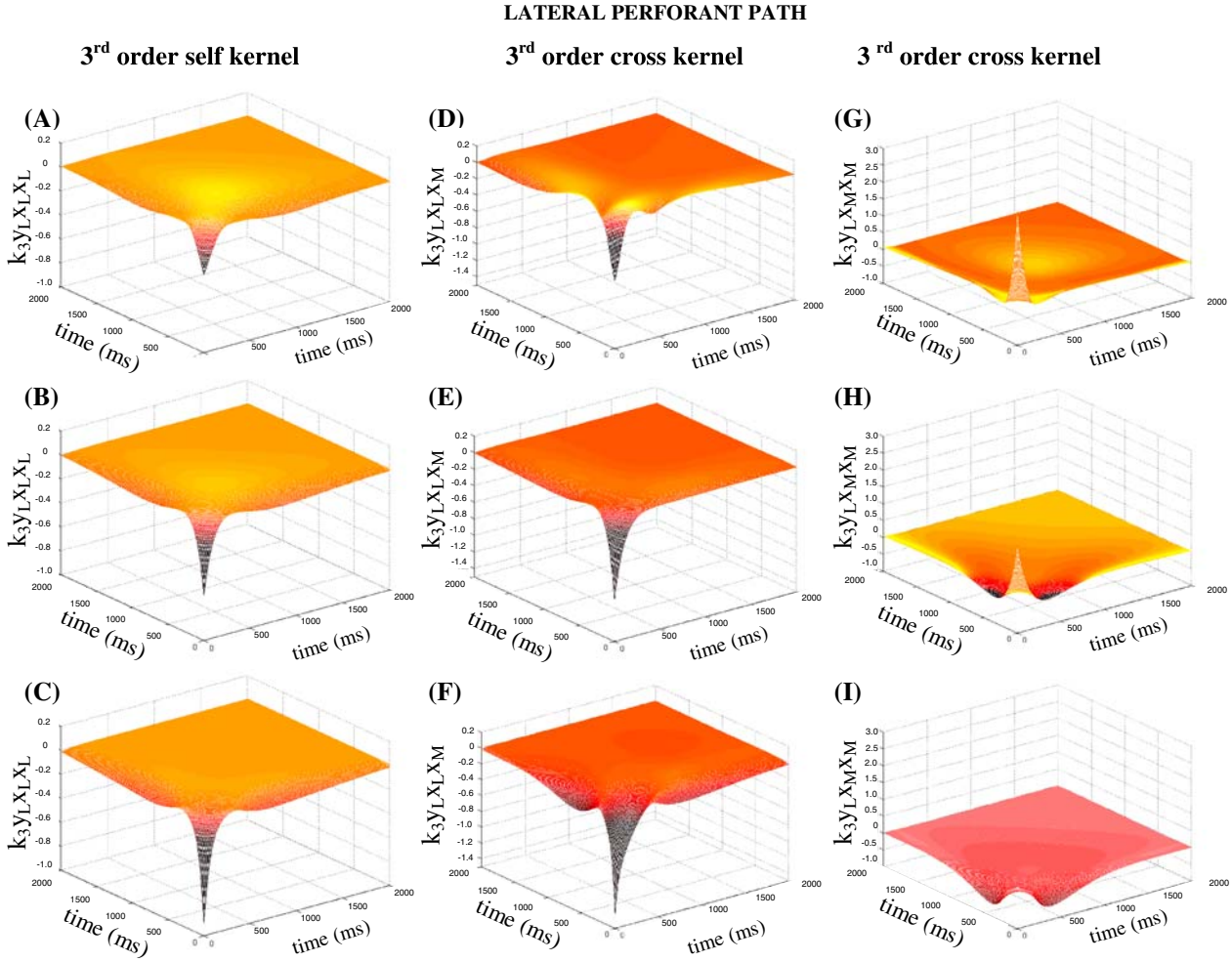

FIGURE 6. The average of the normalized third-order self-kernel for the LPP is shown in panel B on the left column and the standard-deviation bounds are shown in panel A (upper bound—i.e., plus one standard deviation) and C (lower bound—i.e., minus one standard deviation). The averages of the normalized third-order cross-kernels are shown in panels E and H, while the corresponding standard-deviation bounds are shown in panels D and G (upper bounds) and panels F and I (lower bounds).

for the LPP and in Fig. 7 for the MPP. The average values of the normalized third-order LPP self-kernel $k_{3y_Lx_Lx_L}$ are shown in Fig. 6b and the respective standard-deviation bounds are shown in Fig. 6a (upper bound—i.e., average plus one standard deviation) and Fig. 6c (lower bound—i.e., average minus one standard deviation). It is evident in Fig. 6b that this kernel exhibits initially a strong inhibitory region that crosses into two weaker (symmetric) facilitatory regions after 100 ms. The latter regions diminish around 1400 ms. The meaning of the kernel values in the initial inhibitory region is that the effect of a pair of impulses occurring within 100 ms prior to the present impulse is negative on the amplitude of the population spike caused by the present impulse. Conversely, the kernel values in the facilitatory regions indicate that the effect of a pair of impulses occurring between 100 and 1400 ms prior to the present impulse is positive on the amplitude of the population spike caused by the present impulse. The size of this positive or negative effect is determined by the value of the kernel at the coordinates that correspond to the two time-lags of the pair of "conditioning" (i.e., preceding) impulses (i.e., the time between the present output spike and each of the "conditioning" input impulses).

The average values of the normalized third-order LPP cross-kernels $k_{3y_Lx_Lx_M}$ and $k_{3y_Lx_Mx_M}$ are shown in panels E and H, respectively. The corresponding standard-deviation upper bounds are shown in panels D and H, while the lower bounds are shown in panels G and I, respectively. It is evident in Fig. 6e that the cross-kernel $k_{3y_Lx_Lx_M}$ exhibits characteristics similar to the self-kernel in panel B with smaller facilitatory regions. By contrast, we see in Fig. 6h that the cross-kernel $k_{3y_Lx_Mx_M}$ exhibits opposite characteristics (i.e., an initial strong facilitatory region that crosses into

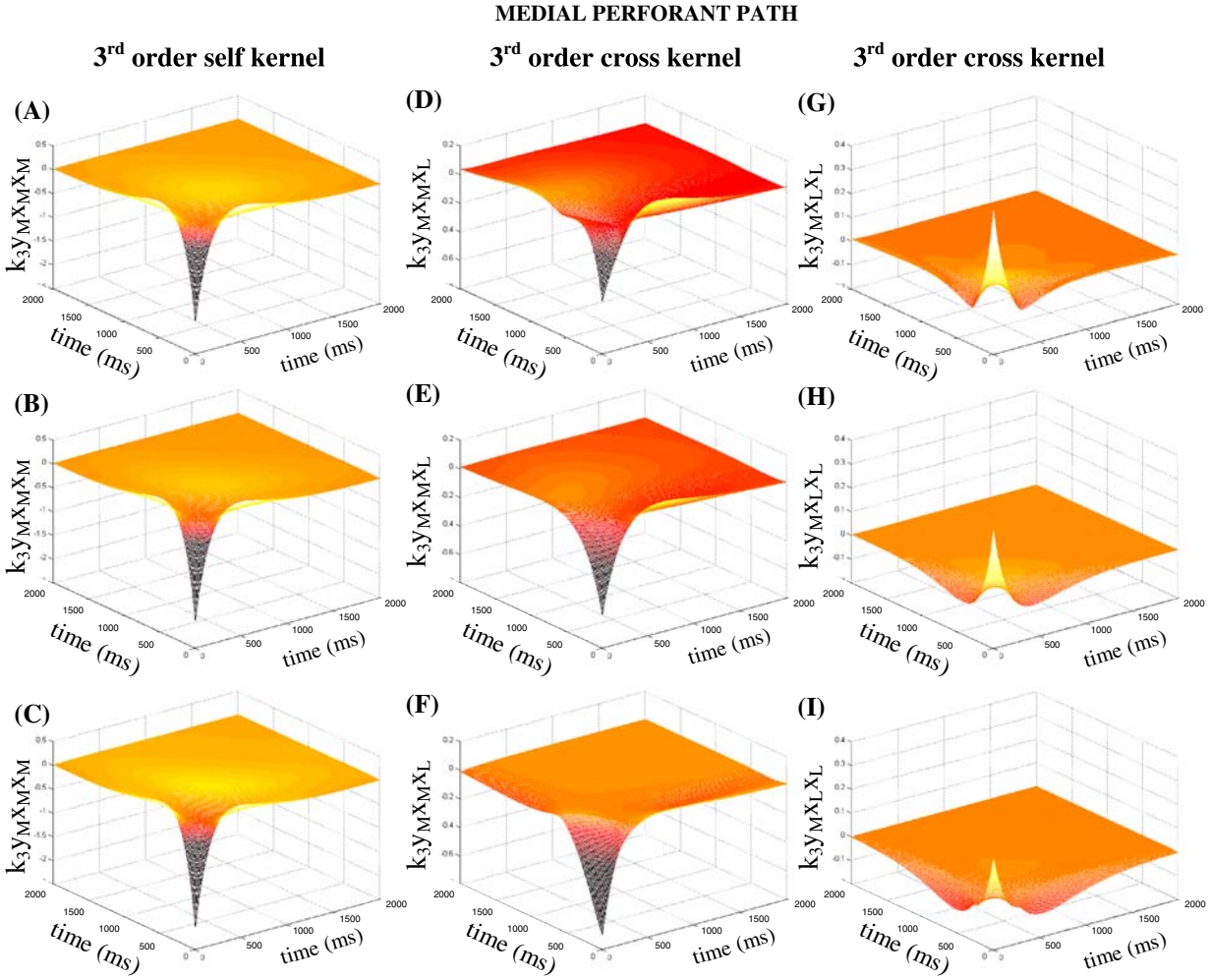

FIGURE 7. The average of the normalized third-order self-kernel for the MPP is shown in panel B on the left column and the standard-deviation bounds are shown in panel A (upper bound) and C (lower bound). The averages of the normalized third-order cross-kernels are shown in panels E and H, while the corresponding standard-deviation bounds are shown in panels D and G (upper bounds) and panels F and I (lower bounds).

two weaker inhibitory regions around 200 ms). Note also that the cross-kernels are not symmetric in general (unlike the self-kernels that are symmetric by definition).

In an analogous manner to the LPP case, the third-order kernels (self- and cross-) in the MPP case are presented in Fig. 7. The average values of the normalized third-order MPP self-kernel are shown in Fig. 7b and the respective standard-deviation bounds are shown in Fig. 7a (upper bound) and Fig. 7c (lower bound). It is evident in Fig. 7b that this kernel exhibits a similar morphology to its LPP counterpart. The same observation holds for the average values of the normalized third order MPP cross-kernels shown in Figs. 7e and 7h, respectively. The corresponding standard-deviation upper bounds are shown in panels D and H while the lower bounds are shown in panels G and I, respectively. It is noted that the magnitudes of the third-order kernels are not similar for the two pathways. Specifically, the magnitude of the MPP self-kernel is larger its LPP counterpart, but this relation is reversed for the cross-kernels of the two pathways.

Predictive Capabilities of the Model

In addition to providing a quantitative description of the nonlinear dynamic characteristics of the system in the form of kernels, the proposed third-order Poisson–Volterra model has predictive capabilities *for arbitrary inputs*. In Fig. 8, we show the actual output data (i.e., the sequence of population spikes in response to independent RIT stimulation at both pathways) and the response predicted by the third-order Poisson–Volterra model for one representative

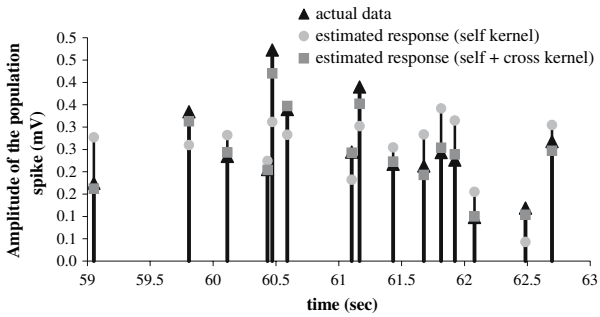

FIGURE 8. The actual output data (▲) and the computed predictions using the third-order model with only the estimated self-kernels (○) and with both the estimated self-kernels and cross-kernels (■).

experiment. Two ways of calculation for the model-predicted response are shown: one considering only the self-kernels and the other considering both the self-kernels and cross-kernels. It is evident that the prediction of the output is better when the cross-kernels are included—a result that suggests that the interactions between the two pathways (captured by the cross-kernels) are significant for this system and must be included in the model. The predictive power of the Poisson–Volterra model can be further validated using out-of-sample predictions, where the system output is predicted for an arbitrary stimulus using kernels obtained from a different input–output dataset (segment shown in Fig. 9). Visual assessment and the computed NMSE values demonstrate the out-of-sample predictive power of the Poisson–Volterra model. For the representative experiment in Fig. 8, the in-sample NMSE is 5.21% and the out-of-sample NMSE is 6.62%.

We should note that, if a second-order Poisson–Volterra model is used (i.e., a model including only first and second order kernels), then the optimum $\alpha = 0.992$ and the model prediction for $L = 3$ has NMSE values of $10.79 \pm 4.48\%$ (when including both self- and cross-kernels). This demonstrates the superiority of the third-order Poisson–Volterra model over the second-order one, since the former yields prediction NMSE values of $5.88 \pm 2.51\%$ ($t = 2.14$, $p < 0.05$, df $= 7$), (a statistically significant reduction).

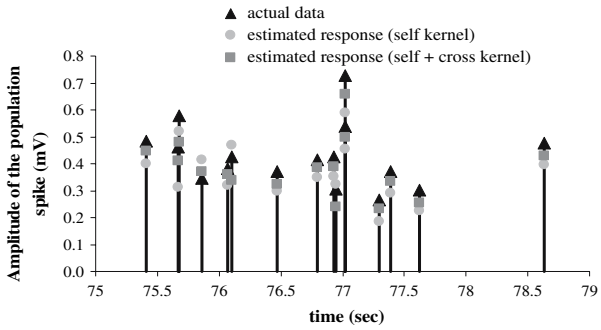

FIGURE 9. The actual output data (▲) and the computed predictions using the third-order model for an out-of-sample dataset (■).

DISCUSSION

Biologically interpretable models of the hippocampus that capture accurately its functional properties and the dynamic interactions among its various neuronal inputs are essential in order to understand how distinct sensory modalities are processed and integrated within the hippocampus. In this study, we use experimental data collected under random stimulation conditions to obtain and validate a non-parametric (Poisson–Volterra) model that describes accurately the effect of the nonlinear dynamic interactions between combined stimulation at the LPP and the MPP pathways on the granule cell activity in the dentate gyrus of the hippocampus. In the presented approach, the functional properties of this hippocampal neuronal network are described reliably and quantitatively by kernel functions that are characteristic of the system and define uniquely its input–output relation so that the output of the system can be accurately predicted in response to arbitrary inputs. These kernel functions are determined experimentally through a novel estimation procedure utilizing data that are collected by stimulating two afferent pathways of the neuronal network (i.e., the LPP and MPP) with random (Poisson) sequences of impulses to generate a broad repertoire of interactions among the network elements. These experimental conditions allow us to observe the activity of the system under a broad variety of operating conditions (over the relatively short experimentation time) that are subsequently analyzed in the general Poisson–Volterra modeling framework to give us the capability of predicting the output for arbitrary inputs (generalization property). The kernels of the obtained Poisson–Volterra model represent a set of canonical descriptors of the functional characteristics of the system and, as such, they can provide some valuable insight into the neuronal mechanisms of this system. However, the non-parametric nature of the model limits its ability to draw a definitive relation with the underlying neuro-molecular structures or mechanisms.

These results demonstrate that the non-parametric (Poisson–Volterra) model captures the nonlinear dynamic interactions between the LPP and the MPP and provides accurate prediction of the system output to arbitrary inputs. It was shown that the inclusion of *third-order* kernels significantly enhances the predictive capabilities of the model and, therefore, the actual

TABLE 1. NMSE comparison for the in-sample second and third order models.

	Second order model (%)	Third order model (%)
Self kernels	19.32 ± 5.21	14.39 ± 3.86
Self & Cross kernels	10.79 ± 4.48	5.88 ± 2.51

system possesses significant third-order nonlinearities (i.e., dynamic interactions among triplets of impulses affect the output) that are ignored in the widely-used approach of paired-pulse stimulation and associated analysis. Specifically, the value of the prediction NMSE dropped by 4.91% ($t = 2.14, p < 0.05, \text{df} = 7$) when the third-order model was used instead of the second-order model. In addition, the inclusion of the *cross*-kernels in the third-order model reduced the prediction NMSE by 8.52% (from 14.39% to 5.88%, $t = 4.13$, $p < 0.01$, $\text{df} = 7$) relative to the respective NMSE value when only the self-kernels were used in the model (not including the pathway interactions) (Table 1). Therefore, the appropriate Poisson–Volterra model that describes the nonlinear dynamic interactions of the two pathways of the perforant path on the granule cell activity of the dentate gyrus is of third-order and must include both the self-kernels and the cross-kernels.

The performance of the third-order model was deemed satisfactory. Although we cannot rule out the possibility of higher order terms, the amount of available data cannot practically support an extension to fourth-order models at this time (without risk of over-fitting). Higher order models will be explored in the future with the use of Principal Dynamic Modes.[41]

Although the application of the RIT stimulation and the analysis of the resulting data in the context of Poisson–Volterra modeling requires greater computational effort, this incremental computational effort is justified by the valuable information contained within the obtained results. This brings us to the perennial question of the physiological significance and the interpretation of the obtained Poisson–Volterra kernels in a manner that advances our scientific understanding of the system. Consider, for instance, the early depressive characteristics of the granule cells that have been attributed to GABA-mediated IPSPs[48] and GABA-mediated increase in chlorium conductance that reduces the excitability of granule cells[23] (for lags less than 40 ms) or have been attributed to the recurrent (feedback) activation of the GABAergic basket cells[5,10,37] (up to lags of 100 ms). Such early negative values (representing depressive effects) are not seen in the obtained second-order kernels but they are evident in the third-order kernels (always in the self-kernels and in one of the two cross-kernels). Our interpretation is that the observed early depression is due to third-order effects in the presence of dual-pathway stimulation (LPP and MPP), while the previously reported observations were for single-pathway stimulation (LPP or MPP).[21] This intriguing result indicates the importance of studying the system of interest under conditions that resemble its normal operation (e.g., combined and random stimulation), otherwise the results may be partial and potentially misleading. Note that the positive values exhibited in the early lags (up to 100 ms) of the second-order kernels may be attributed to NMDA-mediated synaptic events. Similar facilitation characteristics are observed at intermediate lags of the third-order LPP kernel and may be attributed to augmentation of excitatory transmitter release[4,19] or presynaptic inhibition of GABA release.[12,29] This is consistent with the reported facilitation in the region of intermediate lags (100–200 ms). At longer lags (200–1000 ms), the obtained second-order kernels have negative values in agreement with the depressive characteristics of granule cells reported previously[10,13] which may be due to a voltage-dependent and/or calcium-activated potassium conductance.[52,54] These effects are quantitatively reflected on the estimated kernel values and separated into second-order and third-order effects. This initial interpretation of the obtained kernels is only a first step in a long-lasting effort that will be required before complete physiological interpretation can be achieved and the full scientific benefit of this analysis can be realized.

The proposed approach offers the appropriate methodological means for analyzing quantitatively the (nonlinear) dynamic interactions between any two (or more) pathways of the hippocampus or other neuronal systems. Following this approach, future research can expand the mathematical model to include three or more inputs of the dentate gyrus and to incorporate other hippocampal regions. Such a representation of the hippocampus can provide a compact quantitative representation of the interactions among hippocampal pathways (which have been so far studied individually) that may advance our understanding of the complex neuronal mechanisms that integrate sensory information in the hippocampus. This remains a great challenge for future research.

ACKNOWLEDGMENTS

This work was supported in part by NIH Grant No. P41 EB001978 to the USC Biomedical Simulations Resource and NSF Grant No. EEC-0310723 to the USC Engineering Research Center on Biomimetic MicroElectronics Systems.

REFERENCES

[1]Abraham, W. C., S. E. Mason-Parker, M. F. Bear, S. Webb, and W. P. Tate. Heterosynaptic metaplasticity in the hippocampus *in vivo*: a bcm-like modifiable threshold for ltp. *Proc. Natl. Acad. Sci. USA* 98(19):10924–10929, 2001.

[2]Abraham, W. C., and N. McNaughton. Differences in synaptic transmission between medial and lateral components of the perforant path. *Brain Res.* 303(2):251–260, 1984.

[3]Andersen, P., T. V. Bliss, and K. K. Skrede. Unit analysis of hippocampal population spikes. *Exp. Brain Res.* 13(2):208–221, 1971.

[4]Andersen, P., G. N. Gross, T. Lomo, and O. Sveen. Participation of inhibitory and excitatory interneurones in the control of hippocampal cortical output. *UCLA Forum Med. Sci.* 11:415–465, 1961.

[5]Andersen, P., B. Holmqvist, and P. E. Voorhoeve. Entorhinal activation of dentate granule cells. *Acta Physiol. Scand.* 66(4):448–460, 1966.

[6]Berger, T. W., and J. L. Bassett. System properties of the hippocampus. In: Learning and Memory: The Biological Substrates, edited by I. Gormezano and E. A. Wasserman. Lawrence Erlbaum Associates: Hillsdale, NJ, 1992, pp. 275–320.

[7]Berger, T. W., M. Baudry, R. D. Brinton, *et al*. Brain-implantable biomimetic electronics as the next era in neural prosthetics. *Proc. IEEE* 89(7):993–1012, 2001.

[8]Berger, T. W., J. Eriksson, D. Ciarolla, and R. Sclabassi. Nonlinear systems analysis of the hippocampal perforant path-dentate projection. III. Comparison of random train and paired impulse stimulation. *J. Neurophysiol.* 60(3):1095–1109, 1988.

[9]Berger, T. W., J. Eriksson, D. Ciarolla, and R. Sclabassi. Nonlinear systems analysis of the hippocampal perforant path-dentate projection. II. Effects of random impulse train stimulation. *J. Neurophysiol.* 60(3):1076–1094, 1988.

[10]Berger, T. W., T. P. Harty, G. Barrionuevo, and R. J. Sclabassi. Modeling of neuronal networks through experimental decomposition. In: Advanced Methods of Physiological System Modeling, Vol. II, edited by V. Z. Marmarelis. New York: Plenum, 1989, pp. 113–128.

[11]Berger, T. W., T. P. Harty, C. Choi, X. Xie, G. Barrionuevo, and R. J. Sclabassi. Experimental basis for an input/output model of the hippocampus. In: Advanced Methods of Physiological System Modeling, Vol. III, edited by VZ Marmarelis. New York: Plenum, 1994, pp. 29–53.

[12]Brucato, F. H., D. D. Mott, D. V. Lewis, and H. S. Swartzwelder. Gabab receptors modulate synaptically-evoked responses in the rat dentate gyrus, *in vivo*. *Brain Res.* 677(2):326–332, 1995.

[13]Burdette, L. J., and M. E. Gilbert. Stimulus parameters affecting paired-pulse depression of dentate granule cell field potentials. I. Stimulus intensity. *Brain Res.* 680(1–2): 53–62, 1995.

[14]Casti, J. L. Nonlinear System Theory. New York: Academic Press, 1985.

[15]Chon, K. H., T. J. Mullen, and R. J. Cohen. A dual-input nonlinear system analysis of autonomic modulation of heart rate. *IEEE Trans. Biomed. Eng.* 43(5):530–544, 1996.

[16]Colino, A., and R. Malenka. Mechanisms underlying induction of long-term potentiation in rat medial and lateral perforant paths *in vitro*. *J. Neurophysiol.* 69(4):1150–1159, 1993.

[17]Courellis S. H., V. Marmarelis, and T. Berger. Modeling event-driven nonlinear dynamics. In: Annual Conference Biomedical Engineering Society, Seattle, WA, 2000.

[18]Craig, A. D., and D. N. Tapper. A dorsal spinal neural network in cat. III. Dynamic nonlinear analysis of responses to random stimulation of single type 1 cutaneous input fibers. *J. Neurophysiol.* 53(4):995–1015, 1985.

[19]Creager, R., T. Dunwiddie, and G. Lynch. Paired-pulse and frequency facilitation in the ca1 region of the *in vitro* rat hippocampus. *J. Physiol.* 299:409–424, 1980.

[20]Dahl, D., E. C. Burgard, and J. M. Sarvey. Nmda receptor antagonists reduce medial, but not lateral, perforant path-evoked epsps in dentate gyrus of rat hippocampal slice. *Exp. Brain Res.* 83(1):172–177, 1990.

[21]Dimoka, A., S. H. Courellis, G. I. Gholmieh, V. Z. Marmarelis, and T. W. Berger. Modeling the nonlinear properties of the *in vitro* hippocampal perforant path-dentate system using multielectrode array technology. *IEEE Trans. Biomed. Eng.* 55(2):693–702, 2008.

[22]Doyere, V., B. Srebro, and S. Laroche. Heterosynaptic ltd and depotentiation in the medial perforant path of the dentate gyrus in the freely moving rat. *J. Neurophysiol.* 77(2):571–578, 1997.

[23]Eccles, J. N. R., T. Oshima, and F. J. Rubia. The anionic permeability of the inhibitory postsynaptic membrane of hippocampal pyramidal cells. *Proc. R. Soc. Lond. B Biol. Sci.* 198(1133):345–361, 1977.

[24]Eichenbaum, H. The hippocampus and mechanisms of declarative memory. *Behav. Brain Res.* 103(2):123–133, 1999.

[25]Gholmieh, G., S. H. Courellis, A. Dimoka, *et al*. An algorithm for real-time extraction of population epsp and population spike amplitudes from hippocampal field potential recordings. *J. Neurosci. Methods* 136(2):111–121, 2004.

[26]Gholmieh, G., S. H. Courellis, V. Z. Marmarelis, and T. W. Berger. An efficient method for studying short-term plasticity with random impulse train stimuli. *J. Neurosci. Methods* 121(2):111–127, 2002.

[27]Gholmieh, G., W. Soussou, M. Han, *et al*. Custom-designed, high-density conformal planar multielectrode arrays for brain slice electrophysiology. *J. Neurosci. Methods* 152:116–129, 2006.

[28]Harris, E. W., and C. W. Cotman. Effects of synaptic antagonists on perforant path paired-pulse plasticity—differentiation of presynaptic and postsynaptic antagonism. *Brain Res.* 334(2):348–353, 1985.

[29]Harrison, N. L., G. D. Lange, and J. L. Barker. Pre- and post-synaptic aspects of gaba-mediated synaptic inhibition in cultured rat hippocampal neurons. *Adv. Biochem. Psychopharmacol.* 45:73–85, 1988.

[30]Hjorth-Simonsen, A. Projection of the lateral part of the entorhinal area to the hippocampus and fascia dentata. *J. Comp. Neurol.* 146(2):219–232, 1972.

[31]Hjorth-Simonsen, A., and B. Jeune. Origin and termination of the hippocampal perforant path in the rat studied by silver impregnation. *J. Comp. Neurol.* 144(2):215–232, 1972.

[32]Holmes, W. R., and W. R. Levy. Insights into associative long-term potentiation from computational models of nmda receptor-mediated calcium influx and intracellular calcium concentration changes. *J. Neurophysiol.* 63: 1148–1168, 1990.

[33]Kahle, J. S., and C. W. Cotman. Carbachol depresses synaptic responses in the medial but not the lateral perforant path. *Brain Res.* 482(1):159–163, 1989.

[34]Kerr, D. S., and W. C. Abraham. Comparison of associative and non-associative conditioning procedures in the induction of ltd in ca1 of the hippocampus. *Synapse* 14(4):305–313, 1993.
[35]Kitano, K., T. Aoyagi, and T. Fukai. A possible functional organization of the corticostriatal input within the weakly-correlated striatal activity: a modeling study. *Neurosci. Res.* 40(1):87–96, 2001.
[36]Koerner, J. F., and C. W. Cotman. Micromolar l-2-amino-4-phosphonobutyric acid selectively inhibits perforant path synapses from lateral entorhinal cortex. *Brain Res.* 216(1):192–198, 1981.
[37]Lomo, T. Patterns of activation in a monosynaptic cortical pathway: the perforant path input to the dentate area of the hippocampal formation. *Exp. Brain Res.* 12(1):18–45, 1971.
[38]Lynch, G. Synapses, Circuits and the Beginnings of Memory. Cambridge, MA: The MIT Press, 1986.
[39]Macek, T. A., D. G. Winder, R. W. Gereau 4th., C. O. Ladd, P. J. Conn. Differential involvement of group ii and group iii mglurs as autoreceptors at lateral and medial perforant path synapses. *J. Neurophysiol.* 76(6):3798–3806, 1996.
[40]Marmarelis, V. Z. Identification of nonlinear biological systems using laguerre expansions of kernels. *Ann. Biomed. Eng.* 21(6):573–589, 1993.
[41]Marmarelis, V. Z. Nonlinear Dynamic Modeling of Physiological Systems, 1 ed. Wiley-IEEE Press; Engineering IPSoB, ed., 2004.
[42]Marmarelis, V. Z., and T. W. Berger. General methodology for nonlinear modeling of neural systems with poisson point-process inputs. *Math. Biosci.* 196(1):1–13, 2005.
[43]Marmarelis, P. Z., and V. Z. Marmarelis. Analysis of Physiological Systems: The White Noise Approach. New York: Plenum, 1978.
[44]Materne, R., B. E. Van Beers, A. M. Smith, *et al.* Non-invasive quantification of liver perfusion with dynamic computed tomography and a dual-input one-compartmental model. *Clin. Sci. (Lond.)* 99(6):517–525, 2000.
[45]McNaughton, B. L. Evidence for two physiologically distinct perforant pathways to the fascia dentata. *Brain Res.* 199(1):1–19, 1980.
[46]Mc Naughton, B. L., and C. A. Barnes. Physiological identification and analysis of dentate granule cell responses to stimulation of the medial and lateral perforant pathways in the rat. *J. Comp. Neurol.* 175(4):439–454, 1977.
[47]O'Keefe, J., and L. Nadel. The hippocampus as a cognitive map. *Behav. Brain Sci.* 2:487–533, 1979.
[48]Rausche, G., J. M. Sarvey, and U. Heinemann. Slow synaptic inhibition in relation to frequency habituation in dentate granule cells of rat hippocampal slices. *Exp. Brain Res.* 78(2):233–242, 1989.
[49]Sclabassi, R. J., J. L. Eriksson, R. L. Port, G. B. Robinson, and T. W. Berger. Nonlinear systems analysis of the hippocampal perforant path-dentate projection. I. Theoretical and interpretational considerations. *J. Neurophysiol.* 60(3):1066–1076, 1988.
[50]Sclabassi, R., and G. Noreen. The characterization of dual-input evoked potentials as nonlinear systems using random impulse trains. *Proc. Pittsburgh Model. Simul. Conf.* 12:1123–1130, 1981.
[51]Skaggs, W. E., B. L. McNaughton, M. A. Wilson, and C. A. Barnes. Theta phase precession in hippocampal neuronal populations and the compression of temporal sequences. *Hippocampus* 6(2):149–172, 1996.
[52]Steffensen, S. C., and S. J. Henriksen. Effects of baclofen and bicuculline on inhibition in the fascia dentata and hippocampus regio superior. *Brain Res.* 538(1):46–53, 1991.
[53]Steward, O. Topographic organization of the projections from the entorhinal area to the hippocampal formation of the rat. *J. Comp. Neurol.* 167(3):285–314, 1976.
[54]Thalmann, R. H., and G. F. Ayala. A late increase in potassium conductance follows synaptic stimulation of granule neurons of the dentate gyrus. *Neurosci. Lett.* 29(3):243–248, 1982.
[55]Traub, R. D., W. D. Knowles, R. Miles, and R. K. Wong. Models of the cellular mechanism underlying propagation of epileptiform activity in the ca2–ca3 region of the hippocampal slice. *Neuroscience* 21(2):457–470, 1987.
[56]Uva, L., and M. de Curtis. Polysynaptic olfactory pathway to the ipsi- and contralateral entorhinal cortex mediated via the hippocampus. *Neurosci. Lett.* 130(1):249–258, 2005.
[57]Vinogradova, O. S. Functional Organization of the Limbic System in the Process of Registration of Information: Facts and Hypotheses, Vol. 2. New York: Plenum; Pribram RLIaKH, ed. The hippocampus, 1975.
[58]Wang, H., and J. J. Wagner. Priming-induced shift in synaptic plasticity in the rat hippocampus. *J. Neurophysiol.* 82(4):2024–2028, 1999.
[59]White, G., W. B. Levy, and O. Steward. Spatial overlap between populations of synapses determines the extent of their associative interaction during the induction of long-term potentiation and depression. *J. Neurophysiol.* 64(4):1186–1198, 1990.
[60]Wilson, M., and J. M. Bowel. Cortical oscillations and temporal interactions in a computer simulation of piriform cortex. *J. Neurophysiol.* 67:981–995, 1992.
[61]Wilson, R. C., and O. Steward. Polysynaptic activation of the dentate gyrus of the hippocampal formation: an olfactory input via the lateral entorhinal cortex. *Exp. Brain Res.* 33(3–4):523–534, 1978.